Check for updates

Thickness control of 2D nanosheets assembled from precise side-chain giant molecules†

Fengfeng Feng,[a] Dong Guo,[e] Yu Shao,[b] Xiang Yan,[d] Kan Yue,[c] Zhipeng Pan,[a] Xiangqian Li,[a] Dongcheng Xiao,[a] Liang Jin,[a] Wen-Bin Zhang [ID][b] and Hao Liu [ID]*[a]

The performance of 2D nanomaterials hinges on both the chemical compositions and the morphological structures across different length scales. Among all the three dimensions, thickness is the only one that falls into the nanometer scale and, to some extent, determines the intrinsic properties of 2D nanomaterials. In this study, we report the preparation and precise thickness control of 2D nanosheets assembled from a library of monodispersed amphiphilic giant molecules composed of functional polyhedral oligomeric silsesquioxanes (POSSs) as the side groups. Solution self-assembly of such giant molecules resulted in 2D nanosheets with similar structural configurations, where a bilayer of hydrophobic isobutyl POSS (BPOSS) is sandwiched by two monolayers of hydrophilic POSS bearing carboxylic acid groups (APOSS). The thickness of the obtained nanosheets could be tuned through adjusting the chemical compositions of the pendant POSS cages. Intriguingly, we found that the thickness of the 2D nanosheets was not necessarily proportional to the contour length of the giant molecule nor the total number of POSS cages tethered to the main chain. Indeed, the number ratio of BPOSS to APOSS, rather than the exact number, played a deterministic role in the thickness control. To explain the unusual thickness dependence, we built up a structure model with an in-plane orientation of the giant molecules in the nanosheets, from which a formula was further deduced to semi-quantitatively describe the inverse relationship between the overall thickness and the number ratio of BPOSS to APOSS.

Introduction

Two-dimensional (2D) nanomaterials have received broad attention due to their ultrathin planar geometry and the consequent intrinsic physical properties,[1] such as large specific surface area, unique monolayer structure, typical quantum effects and adaptable performance, which jointly boosted their applications in energy storage,[2] adsorption,[3] catalysis[4] and optoelectronics.[5] In particular, the pioneering studies on graphene and graphene-derived materials have shown excellent scientific and economic values,[6–8] which stimulated the exploration of other 2D materials with specific compositions and structures.[9–11] To date, many inorganic 2D nanosheets were prepared by the "top–down" exfoliation method[12] that relied on harsh mechanical or chemical conditions to destroy the physical interactions among stacked layers and turn bulk materials into 2D nanosheets. Another important cluster of 2D nanostructures was prepared through the "bottom–up" assembly approach using sub- to several nanometer-size molecular entities as building blocks under relatively mild conditions.[13–16] Such an assembly approach has provided a complementary variety of unprecedented 2D nanostructures with intriguing structural and physical properties.[17] Since molecular self-assembly depends upon the mutual recognition among collective physical interactions to direct the packing of molecules, the essence of the 2D self-assembly is to locate a particular molecular packing scheme that prefers the formation of 2D over 0D/1D/3D counterparts and meanwhile avoids polymorphic products with different dimensions. Recently, a few prototypes of 2D assemblies have been produced from various building blocks, including small molecules,[18] inorganic nanoparticles, block copolymers,[19,20] programmed peptides[13,21] or peptoids,[19,20,22] *etc.* However, there remains a non-trivial challenge to precisely modulate their structural hierarchy in terms of shape,

[a]State Key Laboratory for Modification of Chemical Fibers and Polymer Materials, Center for Advanced Low-Dimension Materials, College of Materials Science and Engineering, Donghua University, Shanghai 201620, P. R. China. E-mail: liuh@dhu.edu.cn

[b]Key Laboratory of Polymer Chemistry & Physics of Ministry of Education, Center for Soft Matter Science and Engineering, College of Chemistry and Molecular Engineering, Peking University, Beijing 100871, P. R. China

[c]South China Advanced Institute of Soft Matter Science and Technology, School of Molecular Science and Engineering, South China University of Technology, Guangzhou 510640, P. R. China

[d]School of Materials Science and Engineering, Baise University, Baise 533000, P. R. China

[e]Department of Polymer Science, College of Polymer Science and Polymer Engineering, The University of Akron, Akron, Ohio 44325, USA

thickness, lateral size and surface functionality. Tackling these problems requires profound understanding of the packing scheme of molecular building blocks.

Among all the three dimensions of 2D materials, thickness is the only one that falls into the nanometer scale, which brings in numerous special physical properties that root from their ultrathin planar geometry.[23–25] The thickness control of 2D assemblies is of great importance for understanding their self-assembly behaviors and for optimizing their potential properties and functions. To date, the successful thickness modulation of 2D assemblies has only been reported in a few systems. For example, Li[26] and Manners[27–29] used crystalline polymers as building blocks to fabricate 2D platelets with different topologies and tunable surface functionalities. Since the driving force of the 2D platelet formation is the chain-folding crystallization of polymers, temperature is a critical parameter to tune the thickness. Conticello[30,31] and co-workers reported the assembled 2D nanosheets from triple helices of collagen-mimetic peptides that consist of three sequential blocks with positively charged, neutral and negatively charged triads. They managed to increase the thickness of the 2D nanosheets *via* lengthening the triple helix unit through sequential additions of internal triads. In this case, the nanosheet thickness was positively related to the contour length of the building blocks.

Herein, we report a unique thickness control strategy of 2D nanosheets assembled from side-chain giant molecules[32–35] consisting of consecutively connected hydrophobic/hydrophilic polyhedral oligomeric silsesquioxane (BPOSS/APOSS) derivatives as the pendant groups. The selection of POSS-based building blocks is rationalized by their unique preferred arrangement towards 2D aggregates, given a proper driving force.[36,37] For instance, Jiang[38–40] and co-workers were the first to report the 2D assembly of hyperbranched poly(ether amine) containing anthracene moieties and POSS. A self-seeding technique was applied to control the lateral sizes of the nanosheets. However, the authors did not show thickness control of the 2D nanosheets. In this study, we developed a precise synthetic route based on the thiol-maleimide "click" chemistry[41] and "deprotection–addition" cycles[42,43] to build a series of side-chain giant molecules with accurate numbers of POSS-based monomers and predetermined sequences. Notably, such chemical precision is a prerequisite to unambiguously deduce the relationship between the molecular parameters of building blocks and the thickness of their 2D assemblies. Intriguingly, we first found that the nanosheet thickness was decreased when only increasing numbers of BPOSS cages. That is to say, the thickness is not necessarily proportional to the contour length of the giant molecule, nor the total number of POSS cages tethered to the main chain. Furthermore, we revealed that the thickness was dictated by the number ratios of BPOSS to APOSS cages, rather than the exact numbers. We also proposed a schematic structure model and formula to semi-quantitatively explain this unusual behavior. We believe that our systematic study on the 2D self-assembly of precisely defined side-chain giant molecules would prompt a deep understanding on the formation rationale and structural modulation of self-assembled 2D nanostructures, and consequently, guiding the precise structural engineering of 2D nanomaterials towards potential functions and applications.[44–46]

Results and discussion

Synthesis and characterization of the side-chain giant molecules

In the literature, POSS functionalized with various reactive organic groups can be incorporated into virtually any existing polymer system through grafting, copolymerization or blending.[47] Nevertheless, in most studies, the backbones of the POSS–polymer composite are synthesized using traditional polymerization techniques (*e.g.*, free radical polymerization and condensation polymerization), and therefore, at least the molecular weights of the resulting composites are not precise. Inspired by the solid-state synthesis of peptides, Cheng was the first to synthesize chain-like giant molecules with precisely defined sequence and composition by interconnecting POSS of versatile functionalities.[48–50] However, the reported synthetic route suffers from multi-step reactions, tedious purification and low yield of the target products. Here, we propose a combination of the thiol-maleimide "click" reaction and "deprotection–addition" cycles to advance the precise synthesis of chain-like giant molecules.

The general synthetic route and chemical structures of the POSS-based monomers and the resulting giant molecules B_nA (n = 1–5) are depicted in Scheme 1. The details are summarized in the ESI.† Here, the highly efficient and selective thiol-maleimide addition reaction, one of the most used "click" reactions, was exploited to compose the backbone of the linear giant molecules. The monomer **Mal-XPOSS-ST**, where X represents iso-butyl or vinyl groups, was prepared by first coupling a cysteine derivative (**Fmoc-Cys-ST**, *N*-(9-fluorenylmethoxycarbonyl)-*S*-trityl-L-cysteine) with an XPOSS through a routine amidation reaction. After the Fmoc group was carefully deprotected under basic conditions, the maleimide group was then introduced into the amino end. The resulting monomer **Mal-XPOSS-ST** has a reactive maleimide group (Mal) and a dormant trityl-thiol group (ST). The "deprotection–addition" cycle started from **Fmoc-BPOSS-ST** as shown in Scheme 1a. First, the trityl group was deprotected under acidic conditions, generating an active thiol group. The following addition reaction between thiol and maleimide groups was catalyzed by triethylamine. In order to avoid tedious separation associated with lots of COOH groups, an intermediate monomer **Mal-VPOSS-ST** (V denotes vinyl groups) was incorporated into the giant molecules as a precursor of the hydrophilic modification. After completing the synthesis of the target giant molecule, the vinyl groups of VPOSS can be readily transferred into carboxylic acid groups through radical addition by 2-mercaptoacetic acid (see Scheme 1b).

Taking advantage of the "deprotection–addition" cycle, a series of linear giant molecules were feasibly prepared with specific numbers and sequences of BPOSS and APOSS cages. Fig. 1a summarizes the proton nuclear magnetic resonance (^{1}H NMR) spectra from the monomer **Mal-BPOSS-ST** to the intermediate product B_5V (see peak assignments in Scheme S1†).
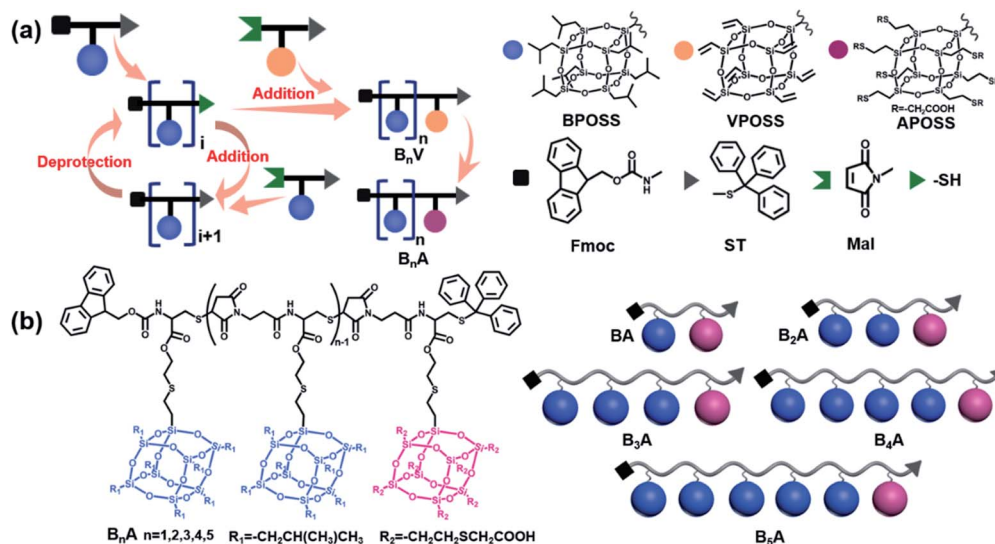
Scheme 1 Synthetic routes and chemical structures of side-chain giant molecules. (a) Illustration of the general "deprotection–addition" cycle to prepare the giant molecules B_nA ($n = 1$–5). The different colors and shapes represent specific POSS species or functional groups. (b) Chemical structures and cartoon illustrations of side-chain giant molecules B_nA ($n = 1$–5). The blue spheres and pink spheres represent BPOSS and APOSS cages, respectively.

Four more intermediate products, **BV–B₄V**, were accordingly synthesized and characterized by gel permeation chromatography (GPC) and matrix assisted laser desorption/ionization-time of flight (MALDI-TOF) mass spectra to confirm the structural precision. All GPC traces (Fig. 1b) of the intermediate B_nV

Fig. 1 Molecular characterization of the giant molecules and the related intermediate compounds. (a) ¹H NMR spectra of molecules from **Fmoc-BPOSS-ST** (denoted as "B" in the spectra) to one final product B_5A. (b) GPC traces and (c) MALDI-TOF MS spectra of B_nV ($n = 1$–5). All the samples in (c) show peaks of [M·Na]⁺ corresponding to the calculated molecular weights.

molecules were symmetric and narrowly distributed, showing the expected gradual shift towards low retention time with increased numbers of POSS cages. Additionally, in the MALDI-TOF mass spectra (Fig. 1c), five single lines exhibiting the measured molecular weights of the corresponding B_nV molecules matched well with the calculated values, providing even starker proof for the successful synthesis and purity of products. Notably, the incorporation of VPOSS at the end of the giant molecule gives rise to the ¹H NMR peaks at around δ 6.2–5.8 ppm. Those peaks totally disappear after all the vinyl groups react with 2-mercaptoacetic acid that transfers B_5V to B_5A. The detailed analysis of the ¹H NMR spectra of other final products (**BA–B₄A**) can be found in Fig. S3.†

Self-assembled 2D nanosheets of the B_nA molecules

To facilitate the solution self-assembly process, a mixture of toluene and *N,N*-dimethylformamide (DMF) was applied to dissolve the B_nA samples, since toluene and DMF are good solvents for BPOSS and APOSS, respectively. 2D nanosheets of B_nA ($n = 1$–5) were readily obtained by placing a small droplet of the sample solution (~0.2 mg mL⁻¹) on a flat substrate and letting it slowly evaporate at ambient temperature. Considering the solubility difference of B_nA ($n = 1$–5), optimization of the initial concentration and toluene/DMF ratio was individually performed (see details in the ESI†). Previously, we reported that the use of a base could deprotonate the carboxylic acid groups on the APOSS cage and result in the formation of 2D nanosheets.[34] Thanks to the lower boiling point and faster evaporation rate of toluene than DMF, the BPOSS cages started to crystallize when the volume fraction of toluene decreased to a critical point. In this study, however, we found that no extra basic species was needed. One possible reason is that the carboxylic acid groups could be partially disassociated in DMF,
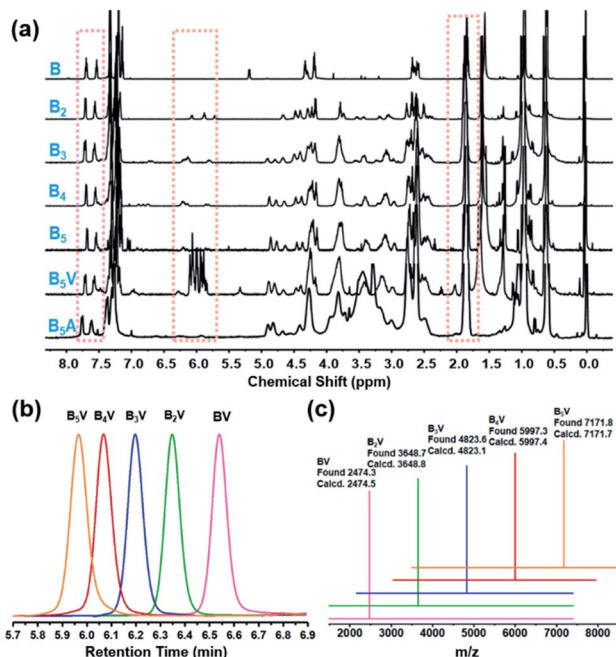
providing electrostatic repulsion to inhibit the growth of the crystalline nanosheets along the normal direction.[51,52] It is also reasonable that the solvation effect between DMF and APOSS cages helps stabilize the 2D nanosheets from physical stacking or aggregation.

The bright-field (BF) transmission electron microscope (TEM) images of the 2D nanosheets assembled from B_nA ($n = 1$–5) are displayed in Fig. 2a. Samples were prepared on carbon-coated mica substrates and then transported to copper grids after the carbon films were floated on a water surface. Obviously, all the samples were able to form discrete 2D nanosheets with the regular parallelogram shape. The lateral size of the nanosheets was around several micrometers. Moreover, atomic force microscopy (AFM) analysis of the nanosheets showed an average thickness of 6.2 ± 0.3 nm, 5.1 ± 0.2 nm, 4.6 ± 0.2 nm, 3.9 ± 0.2 nm, and 3.8 ± 0.2 nm for BA–B_5A, respectively (Fig. 2b). Very interestingly, the observed thickness of the nanosheets gradually decreased as the number of BPOSS cages increased. The change in average thickness from this series of samples was also confirmed using X-ray scattering techniques.

From the grazing incidence wide-angle X-ray diffraction (GIWAXD) data (Fig. 2c), strong diffractions along the substrate normal direction could be observed, which originated from those physically stacked nanosheets. The first order diffraction peaks suggested d-spacing values of 6.40 nm, 4.69 nm, 4.24 nm, 4.07 nm, and 3.95 nm for BA–B_5A, respectively (Fig. 2d). Other diffraction arches were attributed to the inner crystalline BPOSS layers of the 2D nanosheets. The small angle X-ray scattering (SAXS) profiles collected from powder B_nA samples also confirmed the d-spacing values. Although not exactly the same with the thickness values from AFM analysis due to the different measuring principles, the same trend where the thickness of the self-assembled nanosheets decreased with increasing BPOSS numbers could be clearly validated (Fig. 2e).

Structure model construction and thickness formula deduction

From these results and our previous study,[36,37] we hypothesized that such nanosheets were composed of a sandwich-like
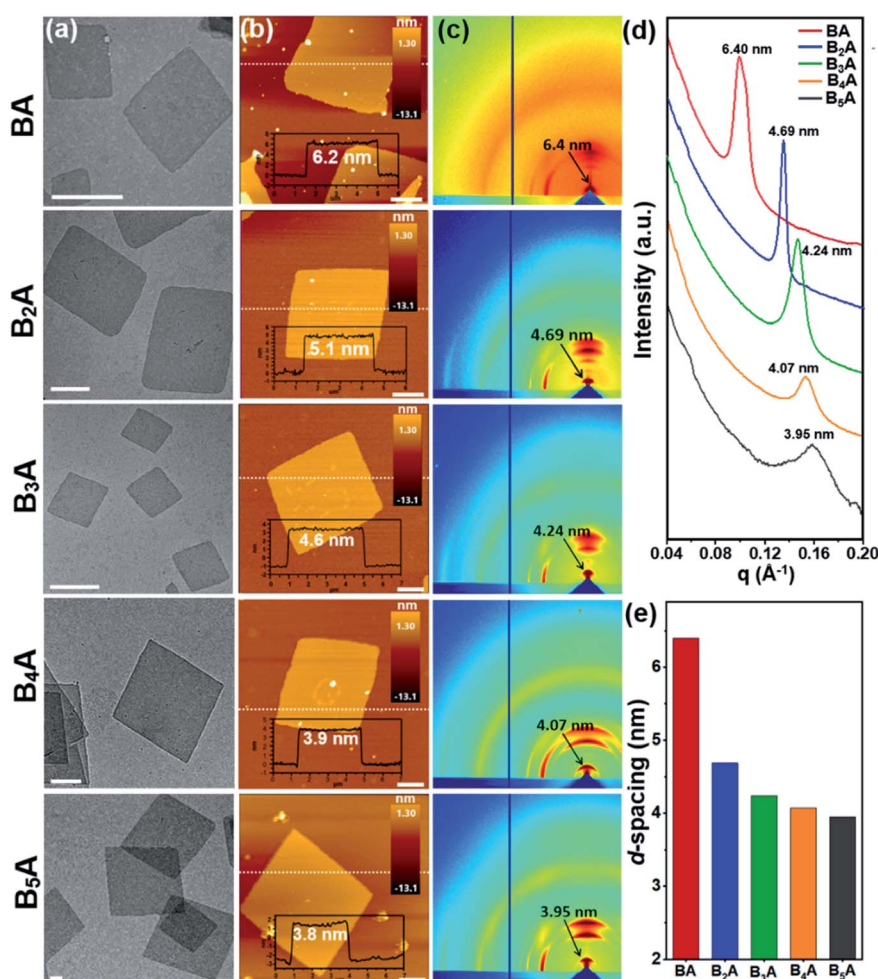

Fig. 2 Characterization of 2D nanosheets assembled from B_nA ($n = 1$–5). (a) TEM BF images of the 2D nanosheets (scale bar = 500 nm). (b) AFM images and height traces of the dashed lines shown as the insets (scale bar = 1 μm). (c) 2D GIWAXD patterns with the d-spacing values assigned to the first order diffraction arches. (d) SAXS profiles collected from powder samples in transmission mode. Intensity is vertically offset for clarity. (e) Histograms of the 2D nanosheet thickness based on the SAXS data in (d).

Table 1 Molecular and structural parameters of side-chain giant molecules and 2D assemblies

Sample	M_{total}^a	$M_b^{a,b}$	N_{BPOSS}	N_{APOSS}	r	h_{AFM}^c	d-Spacing^d	$\Phi_{BPOSS}^{e,f}$	$\Phi_{APOSS}^{e,f}$	$h_{calc.}^{g,f}$
BA	3098.6	455.6	1	1	1	6.2	6.40	29%	43%	6.99
B₂A	4275	403.8	2	1	2	5.1	4.69	41%	31%	4.83
B₃A	5451.2	378.3	3	1	3	4.6	4.24	49%	24%	4.11
B₄A	6627.4	362.7	4	1	4	3.9	4.07	53%	20%	3.75
B₅A	7803.7	352.2	5	1	5	3.8	3.95	57%	17%	3.53
B₂A₂	5885.8	378.3	2	2	1	6.1	6.08	30%	45%	6.65
B₃A₂	7061.7	362.7	3	2	1.5	4.9	4.89	38%	37%	5.32
B₄A₂	8237.6	352.2	4	2	2	4.1	4.57	43%	32%	4.65

^{a} Exact molecular weight (Da). ^{b} The averaged molecular weight of the backbone monomers calculated from total molecular weight of backbone divided by the sum of BPOSS and APOSS numbers. ^{c} The averaged value after measuring 10 individual nanosheets at different locations. ^{d} Calculated from the SAXS patterns using $d = 2\pi/q$. ^{e} Calculated volume fractions of BPOSS and APOSS. ^{f} Calculation carried out by approximating the densities of BPOSS, APOSS and backbone to be 1.25 g cm^{-3}, 1.25 g cm^{-3} and 1.3 g cm^{-3}, respectively. ^{g} Calculated 2D nanosheet thickness.

structure: two layers of crystalline BPOSS covered by two layers of amorphous APOSS/backbone (see the WAXD of APOSS in Fig. S6†). To prove this, selected area electron diffraction (SAED) was utilized to investigate the crystalline structure of the nanosheets. Fortunately, the 3D crystal structure of octaisobutylsilsesquioxane (T8 BPOSS) has already been determined to possess a triclinic unit cell[53] with $P\bar{1}$ space group ($a = 1.00$ nm, $b = 1.08$ nm, $c = 1.10$ nm, $\alpha = 96.54°$, $\beta = 91.27°$, $\gamma = 99.44°$). We further hypothesized that the two BPOSS layers within the nanosheets can be regarded as two crystal planes dragged out from T8 BPOSS's 3D crystals (Table 1).

Computer simulation was then carried out with Accelrys Cerius2 software to calculate electron diffraction (ED) patterns of several possible crystal zones. Fig. 3a and S7† list the crystal packing of T8 BPOSS along the [001], [010] and [100] zones with their corresponding simulated ED patterns (Fig. 3b). Fig. 3c and d display the experimental SAED data collected from **B₃A**, **B₄A**

and **B₅A** nanosheets, respectively. It is quite clear that **BₙA** ($n = 1$–5) shares the same SAED patterns that better match the simulated [001] zone ED pattern after we carefully compare the relative intensities of each diffraction point and reciprocal axis angles (see Fig. S8† for the SAED patterns of **BA** and **B₂A**). Furthermore, wide angle X-ray diffraction (WAXD) was exploited to confirm the crystal structure of inner BPOSS layers of **BA–B₅A** (Fig. S9†). The very similar WAXD patterns with tiny discrepancies, associated with the SAED analysis, indicate that the BPOSS cages in **BA–B₅A** nanosheets take almost the same molecular packing scheme. After clarifying this point, we can go back to explaining the thickness decreasing tendency with increasing BPOSS numbers.

In Fig. 4, we schematically depict the overall 2D nanosheet structures of three samples. It should be noted that the APOSS cages and backbones have no long-range translational or rotational order. Apparently, the total thickness originates from three parts: the crystalline BPOSS bilayers, amorphous backbones and amorphous APOSS layers. As mentioned above, all the nanosheets possess the same crystalline BPOSS bilayers
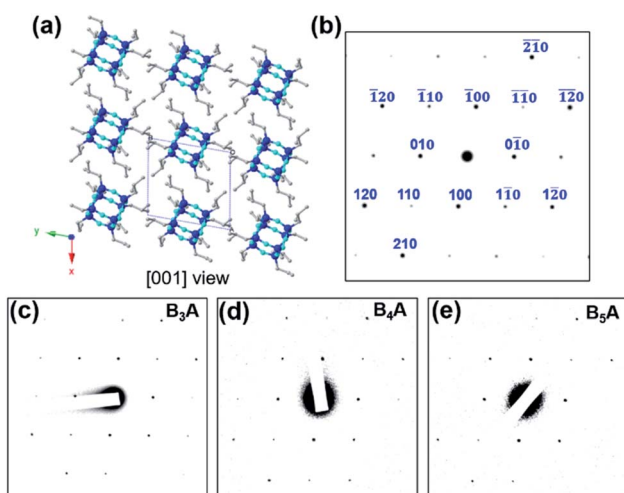

Fig. 3 Structure identification of BPOSS bilayers in the 2D nanosheets. (a) [001] zone view of the crystal lattice model of T8 BPOSS, and (b) the corresponding simulated ED pattern with indices. (c), (d) and (e) are experimental SAED patterns of 2D nanosheets assembled from B₃A, B₄A and B₅A. Color inversion was conducted on the original SAED data for a better contrast.
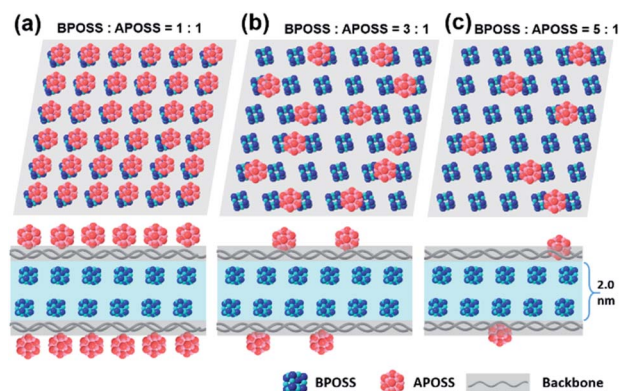

Fig. 4 Representative illustration of the thickness declining tendency with increased number ratios of BPOSS to APOSS. (a), (b) and (c) are top and side views of the proposed structure configurations of BA, B₃A, and B₅A, respectively. Some of the chemical structure details are omitted for clarity. BPOSS layers are crystalline, but APOSS and backbone layers are not supposed to possess any long-range order.

which contribute around 2.0 nm to the total thickness based on its unit cell size. The rest contributions are from the amorphous backbone and APOSS cages. Accounting for the geometry of the nanosheets, a simple calculation gives the following formula of the total thickness h (see detailed deductions in the ESI†):

$$h = 2 \text{ nm} + 2 \text{ nm} \times \left(\frac{(r+1) \times M_b}{r \times \rho_b} + \frac{M_{AP}}{r \times \rho_{AP}} \right) \Big/ \frac{M_{BP}}{\rho_{BP}} \quad (1)$$

where r is the number ratio of BPOSS to APOSS; M_b, M_{AP} and M_{BP} are the molecular weights of the backbone monomer, APOSS and BPOSS, respectively; ρ_b, ρ_{AP}, and ρ_{BP} are densities of the backbone, APOSS and BPOSS, respectively. Notably, M_b is the averaged molecular weight of the backbone monomers after taking into consideration the bulky end groups (*i.e.*, Fmoc and ST). The total thickness h is inversely related to r, which mathematically explains the thickness decreasing tendency. Intuitively, when the ratio r increases from 1 to 5, the extent of congestion among APOSS cages is alleviated (Fig. 4). More accurately speaking, the declined tethering density of APOSS cages on the top and bottom surfaces of BPOSS bilayers leads to the total nanosheet thickness dropping from **BA** to **B₅A**. If we hypothesize that the density of each component stays constant, we can use eqn (1) to calculate the theoretical nanosheet thickness of **BA–B₅A** by approximating the densities of BPOSS, APOSS and backbone to be 1.25 g cm⁻³, 1.25 g cm⁻³ and 1.3 g cm⁻³, respectively (see details in the ESI†). The calculated values are 6.99 nm, 4.83 nm, 4.11 nm, 3.75 nm and 3.53 nm for **BA–B₅A**. Compared to the d-spacing values measured by SAXS in Fig. 2d, the calculated thickness values show the same decreasing tendency with increasing r. Nevertheless, h values are basically overestimated at low r and underestimated at high r. In other words, the densities of the amorphous components are underestimated at low r and overestimated at high r, given that the density of crystalline BPOSS does not change with r. This can be explained by the models in Fig. 4. When $r = 1$ (Fig. 4a), APOSS and the backbone are supposed to have very few free volumes due to the high crowdedness of matters, and thus the densities of both components should be larger than the estimated value. When r increases (Fig. 4b and c), the tethering density of APOSS decreases and the congestion among APOSS cages is gradually released. As a result, the APOSS cages can have larger and larger free volumes to move, and the genuine densities should be declined. That is to say, the density of APOSS is a function of r. This kind of tethering density-induced property change was also discovered in a diblock copolymer single crystal system.

Validation of the structure model by the B$_n$A$_2$ molecules

The models shown in Fig. 4 associated with eqn (1) can reasonably explain our experimental observations on the self-assembly behaviors of the **B$_n$A** molecules. As mentioned in our previous publications,[36,37] the prerequisite of nanosheet formation is that the number of BPOSS in the giant molecule would not be smaller than that of the APOSS. Otherwise, the BPOSS cages cannot crystallize to form the inner bilayers due to the steric hindrance. To prove it, we synthesized **BA₂** and no

nanosheets were obtained from this sample (see details in the ESI and Fig. S10†). Therefore, eqn (1) is only valid when $r \geq 1$. From eqn (1), it can be further concluded that at a fixed number of BPOSS, increasing the number of APOSS will enlarge the total thickness of 2D nanosheets as long as $r \geq 1$ is fulfilled. To test this deduction, three more samples **B₂A₂**, **B₃A₂** and **B₄A₂** were intentionally synthesized (Fig. 5a) and characterized (see details in the ESI†). Their r values are 1, 1.5 and 2, respectively.

The 2D nanosheets for microscopy characterization were accordingly prepared by the abovementioned methods. BF TEM images in Fig. 5b suggest all the three nanosheet samples hold the same parallelogram shapes with lateral size around several micrometers (see SAED patterns in Fig. S8†). AFM measurements in Fig. 5c give the averaged thickness of 6.1 ± 0.2 nm, 4.9 ± 0.2 nm and 4.4 ± 0.2 nm for **B₂A₂**, **B₃A₂** and **B₄A₂**, respectively. The corresponding d-spacing values obtained from SAXS are 6.08 nm, 4.89 nm and 4.57 nm (Fig. 5d), matching well with the AFM results. On the other hand, the d-spacing values of **B₂A**, **B₃A** and **B₄A** are 4.82 nm, 4.23 nm and 3.89 nm (Fig. 2d). A comparative histogram in Fig. 5e directly reflects the enlarged
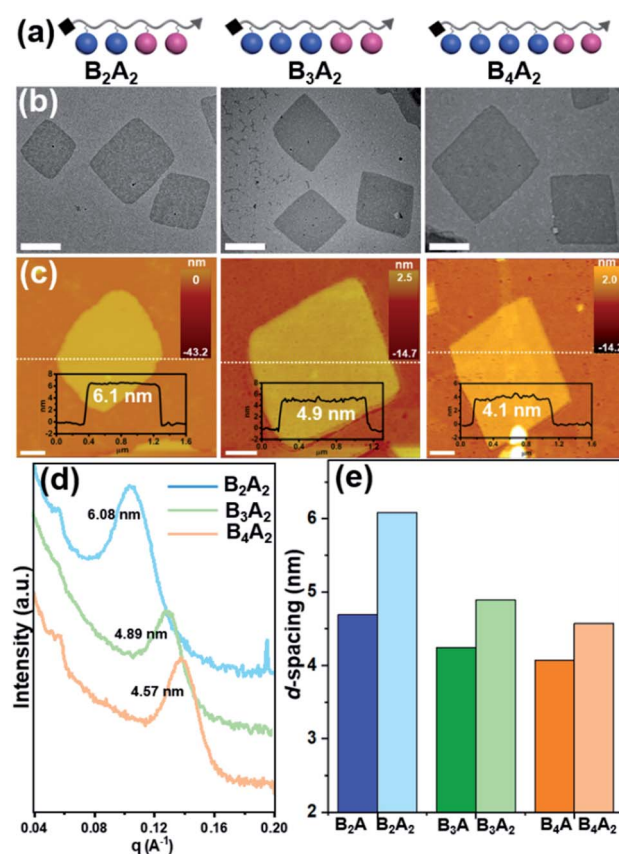

Fig. 5 Characterization of 2D nanosheets assembled from B$_n$A$_2$ (n = 2–4). (a) Cartoon illustrations of side-chain giant molecules B$_n$A$_2$ (n = 2–4). (b) TEM BF images of the 2D nanosheets (scale bar = 500 nm). (c) AFM images and height traces of the dashed lines shown as the insets (scale bar = 1 μm). (d) SAXS profiles collected from powder samples in transmission mode. Intensity is vertically offset for clarity. (e) Histograms of the 2D nanosheet thickness based on the SAXS data in (c) and Fig. 2d.

thickness with increasing APOSS numbers at fixed BPOSS numbers (4.82 nm → 6.08 nm, 4.23 nm → 4.89 nm and 3.89 nm → 4.57 nm). Finally, even at the same r value, the thickness of 2D nanosheets is still affected by the absolute number of backbone monomers. Such an impact can be revealed by comparing the d-spacing values of BA/B_2A_2 (6.40 nm/6.08 nm) and B_2A/B_4A_2 (4.82 nm/4.57 nm). Although the density of the amorphous component is identical with the same r, the averaged M_b values are different for BA/B_2A_2 (456 g mol^{-1}/362 g mol^{-1}) and B_2A/B_2A_2 (378 g mol^{-1}/362 g mol^{-1}). Therefore, the total thickness is also influenced by the two bulky end groups. In the future study, we plan to design sequential or regio-isomers[54,55] to gain a deeper understanding on the counterintuitive molecular packing of these 2D materials.

Conclusions

In summary, a family of precisely defined side-chain giant molecules with different contour lengths and compositions (B_nA_i, $n = 1–5$, $i = 1–2$) were modularly synthesized via the "deprotection–addition" cycle. Under optimized conditions, such giant molecules can self-assemble into 2D nanosheets through a simple solvent evaporation process. Those nanosheets have a sandwich-like structure configuration. We further observed that the thickness of obtained nanosheets was very sensitive to the structural parameters of the side-chain giant molecules, specifically the number ratio of BPOSS to APOSS. For B_nA ($n = 1–5$, $r = 1–5$) with one APOSS located at the chain end, the nanosheet thickness gradually decreases with increasing numbers of BPOSS, as evidenced by AFM, GIWAXD and SAXS measurements. A simple structure model was proposed to explain the variation in thickness, from which a formula was deduced to describe the decreasing tendency of nanosheet thickness with increasing r values. Importantly, this model was reaffirmed by the B_nA_2 ($n = 2–4$) samples. This study has clarified the relationship between the chemical structure of giant molecule chains and the thickness of their 2D assemblies. We believe that this study represents a profound understanding towards the fabrication and structural control of 2D nanostructures via the self-assembly strategy and would also expand our toolbox for structure engineering of 2D functional nanomaterials.

Author contributions

F. F., H. L. and K. Y. designed the studies and prepared the manuscript. D. G. and X. Y. carried out the preliminary synthesis of the monomers. F. F. and Z. P. modified the premature synthetic routes and finished the synthesis/characterization of all samples. F. F. carried out all the AFM tests. TEM characterization, including bright field images and SAED patterns, was conducted by X. L. and D. X. GIWAXD experiments were carried out by D. G. SAXS characterization was finished by Y. S. and W.-B. Z. All GPC experiments were conducted by L. J. Computer simulation was carried out by H. L. All authors discussed the results and commented on the manuscript.

Conflicts of interest

There are no conflicts to declare.

Acknowledgements

References

1 X. Zhang and Y. Xie, Chem. Soc. Rev., 2013, 42, 8187–8199.

2 P. Zhang, F. Wang, M. Yu, X. Zhuang and X. Feng, Chem. Soc. Rev., 2018, 47, 7426–7451.

3 F. Schedin, A. K. Geim, S. V. Morozov, E. W. Hill, P. Blake, M. I. Katsnelson and K. S. Novoselov, Nat. Mater., 2007, 6, 652–655.

4 D. Deng, K. S. Novoselov, Q. Fu, N. Zheng, Z. Tian and X. Bao, Nat. Nanotechnol., 2016, 11, 218–230.

5 A. Splendiani, L. Sun, Y. Zhang, T. Li, J. Kim, C. Y. Chim, G. Galli and F. Wang, Nano Lett., 2010, 10, 1271–1275.

6 Y. Hernandez, V. Nicolosi, M. Lotya, F. M. Blighe, Z. Sun, S. De, I. T. McGovern, B. Holland, M. Byrne, Y. K. Gun'Ko, J. J. Boland, P. Niraj, G. Duesberg, S. Krishnamurthy, R. Goodhue, J. Hutchison, V. Scardaci, A. C. Ferrari and J. N. Coleman, Nat. Nanotechnol., 2008, 3, 563–568.

7 Y. Cao, V. Fatemi, S. Fang, K. Watanabe, T. Taniguchi, E. Kaxiras and P. Jarillo-Herrero, Nature, 2018, 556, 43–50.

8 M. J. Allen, V. C. Tung and R. B. Kaner, Chem. Rev., 2009, 110, 132–145.

9 G. R. Bhimanapati, Z. Lin, V. Meunier, Y. Jung, J. Cha, S. Das, D. Xiao, Y. Son, M. S. Strano, V. R. Cooper, L. Liang, S. G. Louie, E. Ringe, W. Zhou, S. S. Kim, R. R. Naik, B. G. Sumpter, H. Terrones, F. Xia, Y. Wang, J. Zhu, D. Akinwande, N. Alem, J. A. Schuller, R. E. Schaak, M. Terrones and J. A. Robinson, ACS Nano, 2015, 9, 11509–11539.

10 X. Zhang, L. Hou, A. Ciesielski and P. Samorì, Adv. Energy Mater., 2016, 6, 1600671.

11 S. Z. Butler, S. M. Hollen, L. Cao, Y. Cui, J. A. Gupta, H. R. Gutiérrez, T. F. Heinz, S. S. Hong, J. Huang, A. F. Ismach, E. Johnston-Halperin, M. Kuno, V. V. Plashnitsa, R. D. Robinson, R. S. Ruoff, S. Salahuddin, J. Shan, L. Shi, M. G. Spencer, M. Terrones, W. Windl and J. E. Goldberger, ACS Nano, 2013, 7, 2898–2926.

12 J. N. Coleman, M. Lotya, A. O'Neill, S. D. Bergin, P. J. King, U. Khan, K. Young, A. Gaucher, S. De, R. J. Smith,

I. V. Shvets, S. K. Arora, G. Stanton, H.-Y. Kim, K. Lee, G. T. Kim, G. S. Duesberg, T. Hallam, J. J. Boland, J. J. Wang, J. F. Donegan, J. C. Grunlan, G. Moriarty, A. Shmeliov, R. J. Nicholls, J. M. Perkins, E. M. Grieveson, K. Theuwissen, D. W. McComb, P. D. Nellist and V. Nicolosi, *Science*, 2011, **331**, 568–571.

13 L. Liu, L. H. Klausen and M. Dong, *Nano Today*, 2018, **23**, 40–58.

14 K. T. Nam, S. A. Shelby, P. H. Choi, A. B. Marciel, R. Chen, L. Tan, T. K. Chu, R. A. Mesch, B. C. Lee, M. D. Connolly, C. Kisielowski and R. N. Zuckermann, *Nat. Mater.*, 2010, **9**, 454–460.

15 Y. Lin, M. R. Thomas, A. Gelmi, V. Leonardo, E. T. Pashuck, S. A. Maynard, Y. Wang and M. M. Stevens, *J. Am. Chem. Soc.*, 2017, **139**, 13592–13595.

16 W. Bai, Z. Jiang, A. E. Ribbe and S. Thayumanavan, *Angew. Chem., Int. Ed.*, 2016, **55**, 10707–10711.

17 C. E. Boott, A. Nazemi and I. Manners, *Angew. Chem., Int. Ed.*, 2015, **54**, 13876–13894.

18 Y. Kim, S. Shin, T. Kim, D. Lee, C. Seok and M. Lee, *Angew. Chem., Int. Ed.*, 2013, **52**, 6426–6429.

19 B. Li and C. Y. Li, *J. Am. Chem. Soc.*, 2006, **129**, 12–13.

20 M.-S. Hsiao, W. Y. Chen, J. X. Zheng, R. M. Van Horn, R. P. Quirk, D. A. Ivanov, E. L. Thomas, B. Lotz and S. Z. D. Cheng, *Macromolecules*, 2008, **41**, 4794–4801.

21 Y. Lin, M. R. Thomas, A. Gelmi, V. Leonardo, E. T. Pashuck, S. A. Maynard, Y. Wang and M. M. Stevens, *J. Am. Chem. Soc.*, 2017, **139**, 13592–13595.

22 E. J. Robertson, A. Battigelli, C. Proulx, R. V. Mannige, T. K. Haxton, L. Yun, S. Whitelam and R. N. Zuckermann, *Acc. Chem. Res.*, 2016, **49**, 379–389.

23 L. Dou, A. B. Wong, Y. Yu, M. Lai, N. Kornienko, S. W. Eaton, A. Fu, C. G. Bischak, J. Ma, T. Ding, N. S. Ginsberg, L.-W. Wang, A. P. Alivisatos and P. Yang, *Science*, 2015, **349**, 1518.

24 A. Ciarrocchi, A. Avsar, D. Ovchinnikov and A. Kis, *Nat. Commun.*, 2018, **9**, 919.

25 C. Tan, X. Cao, X.-J. Wu, Q. He, J. Yang, X. Zhang, J. Chen, W. Zhao, S. Han, G.-H. Nam, M. Sindoro and H. Zhang, *Chem. Rev.*, 2017, **117**, 6225–6331.

26 B. Li, C. Ni and C. Y. Li, *Macromolecules*, 2007, **41**, 149–155.

27 X. He, Y. He, M.-S. Hsiao, R. L. Harniman, S. Pearce, M. A. Winnik and I. Manners, *J. Am. Chem. Soc.*, 2017, **139**, 9221–9228.

28 X. He, M.-S. Hsiao, C. E. Boott, R. L. Harniman, A. Nazemi, X. Li, M. A. Winnik and I. Manners, *Nat. Mater.*, 2017, **16**, 481–488.

29 Z. M. Hudson, C. E. Boott, M. E. Robinson, P. A. Rupar, M. A. Winnik and I. Manners, *Nat. Chem.*, 2014, **6**, 893–898.

30 A. D. Merg, G. Touponse, E. van Genderen, X. Zuo, A. Bazrafshan, T. Blum, S. Hughes, K. Salaita, J. P. Abrahams and V. P. Conticello, *Angew. Chem., Int. Ed.*, 2019, **131**, 13641–13646.

31 A. D. Merg, E. van Genderen, A. Bazrafshan, H. Su, X. Zuo, G. Touponse, T. B. Blum, K. Salaita, J. P. Abrahams and V. P. Conticello, *J. Am. Chem. Soc.*, 2019, **141**, 20107–20117.

32 W. B. Zhang, X. F. Yu, C. L. Wang, H. J. Sun, I. F. Hsieh, Y. W. Li, X. H. Dong, K. Yue, R. Van Horn and S. Z. D. Cheng, *Macromolecules*, 2014, **47**, 1221–1239.

33 W.-B. Zhang and S. Z. D. Cheng, *Giant*, 2020, **1**, 100011.

34 Y. Liu, T. Liu, X.-y. Yan, Q.-Y. Guo, J. Wang, R. Zhang, S. Zhang, Z. Su, J. Huang, G.-X. Liu, W. Zhang, W. Zhang, T. Aida, K. Yue, M. Huang and S. Z. D. Cheng, *Giant*, 2020, **4**, 100031.

35 G. Li, Z. Gan, Y. Liu, S. Wang, Q.-Y. Guo, Z. Liu, R. Tan, D. Zhou, D. Kong, T. Wen and X.-H. Dong, *ACS Nano*, 2020, **14**, 13816–13823.

36 H. Liu, C.-H. Hsu, Z. Lin, W. Shan, J. Wang, J. Jiang, M. Huang, B. Lotz, X. Yu, W.-B. Zhang, K. Yue and S. Z. D. Cheng, *J. Am. Chem. Soc.*, 2014, **136**, 10691–10699.

37 H. Liu, J. Luo, W. Shan, D. Guo, J. Wang, C.-H. Hsu, M. Huang, W. Zhang, B. Lotz, W.-B. Zhang, T. Liu, K. Yue and S. Z. D. Cheng, *ACS Nano*, 2016, **10**, 6585–6596.

38 B. Yu, X. Jiang and J. Yin, *Macromolecules*, 2014, **47**, 4761–4768.

39 B. Yu, X. Jiang and J. Yin, *Chem. Commun.*, 2013, **49**, 603–605.

40 B. Yu, X. Jiang and J. Yin, *Macromolecules*, 2012, **45**, 7135–7142.

41 D. P. Nair, M. Podgórski, S. Chatani, T. Gong, W. Xi, C. R. Fenoli and C. N. Bowman, *Chem. Mater.*, 2014, **26**, 724–744.

42 Z. Huang, Q. Shi, J. Guo, F. Meng, Y. Zhang, Y. Lu, Z. Qian, X. Li, N. Zhou, Z. Zhang and X. Zhu, *Nat. Commun.*, 2019, **10**, 1918.

43 Z. Liu, Z. Yang, X. Chen, R. Tan, G. Li, Z. Gan, Y. Shao, J. He, Z. Zhang, W. Li, W.-B. Zhang and X.-H. Dong, *JACS Au*, 2021, **1**, 79–86.

44 Z. Li, H. Li, J. Zhang, X. Liu, Z. Gu and Y. Li, *Chin. J. Polym. Sci.*, 2020, **38**, 1149–1156.

45 Z. Li, J. Hu, L. Yang, X. Zhang, X. Liu, Z. Wang and Y. Li, *Nanoscale*, 2020, **12**, 11395–11415.

46 Z. Li, J. Zhang, Y. Fu, L. Yang, F. Zhu, X. Liu, Z. Gu and Y. Li, *J. Mater. Chem. B*, 2020, **8**, 7018–7023.

47 S.-W. Kuo and F.-C. Chang, *Prog. Polym. Sci.*, 2011, **36**, 1649–1696.

48 W. Zhang, M. Huang, H. Su, S. Zhang, K. Yue, X.-H. Dong, X. Li, H. Liu, S. Zhang, C. Wesdemiotis, B. Lotz, W.-B. Zhang, Y. Li and S. Z. D. Cheng, *ACS Cent. Sci.*, 2016, **2**, 48–54.

49 W. Zhang, S. Zhang, Q. Guo, X. Lu, Y. Liu, J. Mao, C. Wesdemiotis, T. Li, Y. Li and S. Z. D. Cheng, *ACS Macro Lett.*, 2018, **7**, 635–640.

50 W. Zhang, X. Lu, J. Mao, C.-H. Hsu, G. Mu, M. Huang, Q. Guo, H. Liu, C. Wesdemiotis, T. Li, W.-B. Zhang, Y. Li and S. Z. D. Cheng, *Angew. Chem., Int. Ed.*, 2017, **56**, 15014–15019.

51 X. Yu, W.-B. Zhang, K. Yue, X. Li, H. Liu, Y. Xin, C.-L. Wang, C. Wesdemiotis and S. Z. D. Cheng, *J. Am. Chem. Soc.*, 2012, **134**, 7780–7787.

52 Y. A. Fadeeva and L. P. Safonova, *J. Solution Chem.*, 2011, **40**, 980–988.

53 A. R. Bassindale, Z. Liu, I. A. MacKinnon, P. G. Taylor, Y. Yang, M. E. Light, P. N. Horton and M. B. Hursthouse, *Dalton Trans.*, 2003, **14**, 2945–2949.

54 Y. Shao, S. Yang and W.-B. Zhang, *Chem.–Eur. J.*, 2020, **26**, 2985–2992.

55 X.-M. Wang, Y. Shao, P.-F. Jin, W. Jiang, W. Hu, S. Yang, W. Li, J. He, P. Ni and W.-B. Zhang, *Macromolecules*, 2018, **51**, 1110–1119.